2012

Carbon Nanotube Coatings for Enhanced Capillary-Fed Boiling from Porous Microstructures

J. A. Weibel
Purdue University, jaweibel@purdue.edu

S. S. Kim
Purdue University

T. S. Fisher
Purdue University

S V. Garimella
Purdue University, sureshg@purdue.edu

Weibel, J. A.; Kim, S. S.; Fisher, T. S.; and Garimella, S V., "Carbon Nanotube Coatings for Enhanced Capillary-Fed Boiling from Porous Microstructures" (2012). *CTRC Research Publications.* Paper 170.
http://dx.doi.org/10.1080/15567265.2011.646000

Carbon Nanotube Coatings for Enhanced Capillary-fed Boiling from Porous Microstructures

J. A. Weibel, S. S. Kim, T. S. Fisher and S. V. Garimella*

School of Mechanical Engineering and Birck Nanotechnology Center
Purdue University, 585 Purdue Mall, West Lafayette, IN 47907, USA

ABSTRACT

Owing to their high intrinsic thermal conductivity, carbon nanotubes (CNTs) have previously been incorporated into a variety of thermal management applications to improve cooling performance. Implementation of controlled CNT growth techniques and functionalization methods are applied herein to enhance boiling heat transfer from the porous capillary wicking surfaces widely used in high heat flux thermal management devices. A microwave plasma chemical vapor deposition (MPCVD) synthesis process resulted in growth of a permeable CNT coating, and physical vapor deposition of copper over these nanotubes yielded the requisite hydrophilic wicking surface. An array of test samples was fabricated and then evaluated using an experimental test facility to determine the reduction in surface temperature resulting from CNT coating and micropatterning of the porous surfaces under two-phase heat transfer conditions with water as the working fluid. Both CNT coating and micropatterning techniques were able to provide significant performance enhancements, reducing the surface superheat up to 72% compared to baseline tests and eliminating disadvantageous temperature overshoot corresponding to boiling incipience. Such performance gains are attributable to the formation of nanoporous cavities which increase nucleation site density and high permeability vents through which vapor can readily depart the surface under vigorous boiling conditions. The synthesis procedures developed which result in the observed enhancement can be readily incorporated into currently employed devices.

KEY WORDS

carbon nanotubes, microporous materials, microwave plasma-enhanced CVD synthesis, heat transfer, wetting

* To whom correspondence should be addressed: Tel. 1 765 494 5621 ; sureshg@purdue.edu

INTRODUCTION

Advances in controllable synthesis techniques continue to further enable the use of carbon nanotubes (CNTs) in numerous engineering applications that exploit their excellent thermal, mechanical, and electrical properties, even beyond the original set of applications that ensued following their widespread study in the early 1990s [1]. Integrated use of CNTs for thermal management of heat dissipation from electronic devices has been extensively explored due to the extremely high thermal conductivity of CNTs determined both theoretically [2,3] and experimentally [4-8], and has led to the enhancement of multiple technologies spanning the consumer, military, and automotive electronics industries. Such applications include reduction of thermal resistance at interfaces between components [9-13], development of novel composite materials with increased thermal conductivity [14-17], and improvement of pool boiling heat transfer [18-21]. Increasingly high-density heat dissipation from next-generation electronics motivates further investigation of novel heat transfer enhancement strategies which can be readily integrated into practical devices.

A vapor chamber heat spreader (Figure 1) transports heat from a high-density source (that typically cannot be cooled using conventional air-cooling methods) to a low-density, large-area heat rejection surface. Such a device operates passively by transporting the working liquid through a porous material by capillary action to the evaporator surface where evaporation or boiling occurs and heat is absorbed. Pressure generated in the evaporator region forces vapor towards the condenser region, where heat is rejected to the surface and condenses back to a liquid. Nearly isothermal operation of the device at the fluid saturation temperature results in a high effective thermal conductivity that is widely exploited in the electronics cooling industry. However, performance can be limited by a large temperature drop through the evaporator when high heat fluxes are encountered. In order to handle increasingly high heat fluxes dissipated by electronics, the thermal resistance of the vapor chamber device must be reduced; this may be achieved through intelligent integration of CNTs into the evaporator.

While CNT coating of surfaces has been shown to improve pool boiling heat transfer coefficients [18-22], the mechanism is fundamentally different from the phase-change processes that occur in a vapor chamber. In contrast to nucleation of bubbles from a submerged porous substrate in pool boiling, a liquid-vapor free surface exists at the top layer of the porous structure in a vapor chamber, which allows for intensive thin film evaporation and reduced bubble departure resistance. Additionally, the process of capillary wicking of fluid through the porous

material is heavily influenced by bubble nucleation within the wick. Several recent studies [23-26] have described test facilities specifically intended to replicate and investigate this capillary-fed boiling phenomenon from conventional porous wick structures. Yet, enhancement through the use of CNTs is relatively unexplored. In order for CNTs to be widely incorporated, they must be proven to be capable of wicking water, the working fluid with the highest heat transfer potential at the operating temperatures of vapor chambers used to cool electronic systems. Though CNTs are naturally hydrophobic [27-30], surfactants have been shown to facilitate their use as microfluidic capillary pumping devices [31]. A more desirable functionalization method is uniform coating of the individual nanotubes with copper [32-34]. In addition to yielding a wetting surface, using copper – the most widely used wick material – for the coating offers proven long-term reliability and compatibility with the working fluid. The copper coating also adds mechanical support to the CNTs, preventing collapse of the array into bundles when subjected to capillary forces.

In our recent studies, thermal performance of a CNT-coated evaporator was evaluated [34]. The array density and copper coating thickness were varied, and the parameters that resulted in the minimum thermal resistance were identified. A subsequent fluid flow analysis [35] revealed that the low permeability of a dense CNT array limits capillary feeding over large distances and prevents use of such an array over large evaporator areas. To remedy this limitation, a novel evaporator concept was developed with localized CNT array nanowick areas fed by interspersed sintered powder microwick conduits that have higher permeability for bulk fluid flow. A drastic reduction in the evaporator thermal resistance was predicted upon the optimization of the areas covered by the nano- and microwick regions. The current study aims to utilize optimal CNT array parameters and experimentally evaluate the efficacy of this evaporator concept compared to a conventional, homogeneous sintered power wick. Wick samples are fabricated to study the individual as well as combined effects of CNT growth on sintered powder wicks and patterning of sintered powder wicks. This report presents a detailed characterization of the resulting wick nanostructures and measurement of the thermal resistances of the different samples via testing in a capillary-fed boiling facility.

CNT ENHANCED EVAPORATOR STRUCTURES

The design of a CNT wick evaporator structure requires optimization of the CNT array geometry in order to balance two opposing wick characteristics – permeability and capillary pressure. As the array density increases

and the intervening pores become smaller, the flow permeability decreases, and pressure drop through the array inhibits fluid feeding of the evaporator. Alternatively, if the pores are too large, the capillary pumping pressure developed in the wick may be insufficient to drive adequate liquid flow to the heated region. Therefore, development of such evaporator structures requires controllable CNT synthesis conditions with well-understood effects on the corresponding CNT morphology. The microwave plasma-enhanced chemical vapor deposition (MPCVD) process allows for accurate control over the local gas chemistry, catalyst preparation, and bias voltage which can be tuned for variation of CNT array density [36,37]. Investigation of the effects of chemical vapor deposition CNT synthesis process parameters on resulting growth has been similarly engineered various applications [38-40].

Four different wick samples are fabricated to independently study the enhancement provided by several proposed augmentation features. A homogeneous bare sintered powder sample (Figure 2a) serves as the baseline for comparison against a CNT-coated homogeneous sample (Figure 2b), a micropatterned sample (Figure 2c), and a sample having both proposed augmentation features (Figure 2d). The sintered powder features for all samples were created using the same fabrication process, and the CNT growth and functionalization processes used for the coated samples were identical.

Sintered Copper Powder Microwick Fabrication

The first step in sample fabrication is sintering the copper powder microwick and attaching it to a solid substrate that represents the vapor chamber wall. The 25.4 x 25.4 x 0.5 mm solid substrates are composed of laminated 13% Cu, 74% Mo, 13% Cu sheets. This material is chosen for direct mounting of vapor chambers on electronic devices because it matches the thermal expansion coefficient of silicon. The porous wicks are fabricated at Thermacore Inc. by placing copper particles into a mould of the desired pattern and exposing to a proprietary high-temperature forming gas atmosphere to sinter the particles to one another and to the substrate. The resulting structure has a volumetric porosity of 50%. Particles of 100 μm average diameter are used for all samples, yielding approximate pore radii of 21 μm and a permeability of 4.1×10^{-11} m^2 as predicted by correlations for sintered particles [41]. A separate investigation was performed by Bodla *et al.* to determine the capillary properties of such sintered wicks (produced using the same fabrication process) without the use of empirical correlations [42]. Two different wick geometries are fabricated – a homogeneous uniform layer and a square grid pattern – for testing with and without integrated CNT growth. The sintered layers in both geometries are 1 mm thick and cover the central 20.3 x

20.3 mm of the 25.4 x 25.4 mm substrate; this leaves a flat surface along the edges of the porous wick for sealing against the test chamber wall. The patterned sample has a 4 x 4 grid of 1.119 x 1.119 mm open areas separated by 0.508 mm thick sintered channels, in total covering a 6 x 6 mm area above the heat input area (Figure 3). The homogeneous wick does not have a grid pattern and is uniformly coated.

CNT Growth Procedure

For the samples enhanced with CNTs, a trilayer metal catalyst composed of 60 nm of Ti, 10 nm of Al, and 3 nm of Fe was deposited directly on the sintered copper samples using a Leybold e-beam deposition system. The Fe provides active growth sites for the CNTs. The CNTs were grown on the catalyzed samples in a SEKI AX5200s MPCVD system. The system (Figure 4) allows independent control of substrate temperature, substrate position, gas flow rates, chamber pressure, bias voltage and microwave power. The ability to control these independent parameters before and during the growth process leads to the controlled synthesis of CNTs. Details of the CNT growth procedure are available in prior work [36]. In brief, once the samples are introduced, the system was pumped down to 2 Torr. The temperature was ramped to 900 °C under 10 Torr of N_2 for annealing, and growth was initiated under 50 sccm of H_2 and 10 sccm of CH_4. After growth, the system was allowed to cool, and the sample was then removed and observed via scanning electron microscopy.

CNT Functionalization

Initially, a sessile-drop method was used to qualitatively assess the hydrophobicity of the CNT enhanced samples. A water droplet with a macroscopic contact angle greater than 90° formed on the sample surface and there was no observable wicking of the water into the sample. This problem was alleviated by coating the post-CNT-growth sample with a thin layer of evaporated Cu via physical vapor deposition, making the CNT surface hydrophilic. Based on analysis via transmission electron microscopy (Figure 5) of a preliminary sample coated with Cu, it can be inferred that the actual Cu coating thickness for samples used in this work is on the order of tens of nanometers. Qualitative wicking tests conducted after the Cu coating showed water to be instantly wicked into the sample surface, leaving no droplet on the surface.

Resulting Sample Morphology

Observations of the resulting CNT growth for both patterned and homogeneous samples were made via scanning electron microscopy (SEM). Figure 6 presents low, medium and high magnification images of the CNT-coated homogeneous sample following copper deposition. The low magnification image (Figure 6a) highlights the

general topography of the homogeneous sample surface, confirming that the entire bulk porous sintered powder structure is coated with CNTs wherever the trilayer catalyst was deposited. Closer inspection of a single sintered particle at medium magnification (Figure 6b) shows that the top layer of individual particles is coated with CNTs within the SEM field of view. The line of sight catalyst deposition process likely prevents uniform CNT coating around the entire underside of the particles; nonetheless, CNT growth is observed on the vertical sides of the particle and penetrates to particles in the deeper layers within the sintered powder structure. The CNT array structure resulting from the optimized growth recipe is composed of random, non-aligned nanotubes which form a matrix of permeable nanoporous cavities. The formation of CNT nanopores over a large portion of the sintered powder surface is expected to increase the effective heat transfer area from the wick base to the liquid-vapor interface, while simultaneously providing an increased nucleation site density for boiling. The high magnification image (Figure 6c) illustrates the effectiveness of the copper functionalization method. Physical vapor deposition of copper coats each nanotube along the entire tube length and tube diameter resulting in a hydrophilic porous structure that can behave as a capillary wick.

Similar low, medium, and high magnification images of the CNT-coated patterned sintered powder sample are shown in Figure 7. In this case, the images are shown prior to copper deposition and functionalization of the CNTs. No effort was made to mask the catalyst to any specific area, and therefore, CNT growth was observed over the entire patterned sample surface (Figure 7a). By coating with CNTs in this manner, the sintered copper powder sections retain any enhancement provided by the CNTs as with the homogeneous sample, while the exposed substrate at the base of the grid pattern also serves as a wicking surface. Figure 7b shows an individual particle in the sintered powder region of the patterned sample. Similar conclusions can be made about the growth coverage area as observed for the homogeneous sample, but in these images the CNTs have not yet been coated with copper. The images suggest that the CNT array is more tightly packed prior to copper coating as the nanotubes are formed into bundles. The copper coating may thus also serve as a mechanical support to the CNT structure, separating the individual tubes through intermolecular repulsion and preventing collapse of CNTs into bundles. Growth of an aligned CNT array directly on the substrate within the open patterned grid is also confirmed (Figure 7c). This CNT array serves as additional area for evaporation/boiling from a liquid wicking surface compared to the uncoated patterned sample.

PERFORMANCE CHARACTERIZATION

Capillary-fed Boiling Test Facility

To compare heat transfer performance of the four samples, all are tested in a capillary-fed boiling experimental facility which replicates the liquid capillary feeding mechanism and internal conditions of a vapor chamber. All of the boiling curves presented for performance comparison between the multiple evaporator samples were generated using the experimental apparatus and procedures described below. The facility was developed to measure the substrate temperature of a porous wick material subjected to varying heat fluxes as water is fed by capillary action over the sample surface, mimicking the evaporation/boiling mechanisms and boundary conditions that would occur in a vapor chamber [23].

Directly prior to testing, all samples are placed in a hydrogen reduction plasma in the MPCVD chamber at 100 °C for 5 minutes under a plasma power of 200 W to remove any minor copper oxidation and preserve the surface wetting characteristics. In order to supply a high heat flux input to the back of the evaporator substrate, each sample is soldered to a copper heater block with a heat source area of 5 x 5 mm. The heater block is encased in a ceramic insulating shell. The 0.102 mm thick Pb-Sn (conductivity, k_s, 50 W m^{-1} K^{-1}) solder joint is formed in an inert argon environment at 200 °C to prevent surface oxidation. The copper heater block and sample assembly is sealed vertically against the test chamber (Figure 8a). The test chamber contains a bath with a liquid surface level precisely fixed 8.25 mm beneath the heat input area, thereby forcing the liquid to wick over the evaporator to cool the surface. The liquid water bath and vapor space in the chamber are held at the saturation temperature (100 °C) at atmospheric pressure, monitored by internal thermocouples and a pressure transducer. A rigid borescope is sealed through the chamber wall and is attached to a Photron Fastcam-X 1024 PCI high-speed camera to allow for *in situ* visualization of the sample surface during testing at up to 10,000 frames per second. This apparatus can be used to view normally and at a 45° angle to the sample surface, allowing the vapor formation regimes (i.e., evaporation versus boiling) to be identified during testing as discussed in the results section.

To begin an experiment, the water in the chamber is first boiled vigorously with the Graham condenser valve open in order to purge all non-condensable gases and produce a saturated water vapor environment. For each heat flux test point, the required electrical input to the embedded cartridge heaters is provided and the system is allowed to stabilize until the substrate temperature varies less than 0.1 °C min^{-1} for a period of 10 minutes, defined as steady state. Once steady state is reached, the high-speed camera is used to record the corresponding evaporation

or boiling process for every heat flux data point shown on the boiling curve. Each heat flux versus temperature point on the boiling curve is generated from time-averaging 5 minutes of steady-state data. The temperature drop along an array of thermocouples (T_1 to T_4) embedded along the centerline of the copper heater block (Figure 8b) is used to determine the heat flux *q"* according to Fourier's Law for one-dimensional heat flow. This calculation method allows a determination of the actual heat flux, and accounts for heat losses from the heater block insulation. The substrate temperature $T_{substrate}$ is found by extrapolating the measured temperatures to the substrate and accounting for the temperature drop across the solder joint according to

$$T_{substrate} = T_4 - q''\left[\frac{(x_5 - x_4)}{k_{Cu}} + \frac{t_s}{k_s}\right] \quad (1)$$

where x is the thermocouple location, t_s is the solder thickness, and the copper conductivity k_{Cu} is taken as 400 $Wm^{-1}K^{-1}$. An uncertainty analysis reveals the uncertainties in heat flux and substrate temperature; inputs to the uncertainty analysis include the following contributions: ± 0.3 °C thermocouple temperature, ± 0.08 mm thermocouple location, ± 25% solder thickness, ± 5% solder conductivity, and ± $1x10^{-4}$ mm^2 heat input area.

Experimental Results and Discussion

Evaporator performance is determined by the ability of a sample to maintain a low sample substrate temperature for a given heat input. A boiling curve, which plots heat input versus substrate temperature, is developed for each sample by monitoring this temperature over a range of increasing operating heat fluxes. A shift in the boiling curve toward lower surface temperatures indicates an increase in the evaporation/boiling heat transfer coefficient.

All boiling curve results are presented in comparison to the baseline sample A, a uniform homogeneous sintered powder wick, which represents the current standard of performance in vapor chamber devices. Therefore, it is important to first understand the boiling curve and underlying associated heat transfer mechanisms for this sample as represented by the circular data points in Figure 9a. At low heat fluxes, from 13.8 - 53.4 W cm^{-2}, a linear temperature rise is observed with increasing heat flux, corresponding to the evaporation regime. At these heat fluxes, liquid completely saturates the porous structure, and heat transfer occurs through evaporation from the menisci formed at the highest particle layer. A further increase in the heat flux causes incipience of boiling and a substrate temperature drop. We also note that while the boiling curve presents only steady-state data, Figure 9b illustrates the transient temperature response associated with boiling incipience. The temperature drop is nearly

instantaneous as a 6.4 °C decrease is observed between neighboring data points with a sampling rate of 3 per second. This performance increase can be attributed to transition from evaporation at the top particle layer to bubble nucleation at the base of the wick, consequently bypassing conduction resistance through the saturated wick layer [23]. Following incipience, from 70.4 - 514.0 W cm^{-2}, a linear temperature dependence on heat flux is again observed during the boiling regime, albeit with an increased slope attributable to the more effective heat transfer mechanism. This maximum heat flux does not represent a physical sample limitation; instead the experimental facility limits tests at higher heat fluxes. This is the case for all results presented in this study.

To evaluate and isolate the effects of a CNT coating grown over a copper sintered powder wick on vapor chamber evaporator performance, the CNT-coated homogeneous wick boiling curve is compared against the uncoated wick in Figure 9a. The CNT coating augments performance primarily at low heat fluxes. Unlike the uncoated sample, boiling incipience occurs immediately at the first test heat flux of 19.3 W cm^{-2}. Therefore, the substrate temperature immediately follows the steeper linear slope associated with boiling and provides lower-temperature operation up to the heat flux at which incipience occurs in the uncoated sample. This enhancement results in a substrate temperature reduction compared to the uncoated sample of as much as 6.4 °C at 57.5 W cm^{-2}, a 72% decrease in the substrate superheat. Once the heat flux reaches and exceeds approximately 70 W cm^{-2}, the performance is similar for the CNT-coated and uncoated samples within experimental uncertainty.

Similar enhancement has been observed for pool boiling where CNT-[20] and copper nanowire-[22] coated copper surfaces reduced the incipience superheat associated with transition from free convection to nucleate boiling due to an increased availability of cavities for vapor embryo entrapment and nucleation. This CNT-enhancement phenomenon has not been previously identified for transition from evaporation to boiling in capillary-fed porous media. Uniform coating of sintered copper particles with a random mesh CNT array breaks up the liquid-vapor free interface and creates a large number of potential nanoscale vapor nucleation sites over the submerged particles. This nanostructuring forces transition to the more efficient boiling process in a capillary-fed porous material which otherwise would sustain evaporation up to moderately large heat fluxes (which represent the typical regime of operation for lower power electronics). In addition to the reduction in substrate temperature at low heat fluxes, the elimination of a large, sudden and unpredictable temperature drop as typically seen due to temperature overshoot in uncoated sintered materials is highly advantageous for regulation of temperature-sensitive electronic devices which are susceptible to fast thermal transients.

Performance of the micropatterned sintered powder wick, sample C, featuring a 4 x 4 grid of square-cut holes exposing the underlying substrate is compared against the homogeneous sample A. There are two motivating hypotheses behind patterning of the sintered powder wick. The first involves the intentional creation of small regions on the exposed substrate over which CNTs arrays can be grown. The small nanowick evaporator surfaces thus created do not suffer from the large pressure drops encountered if the entire substrate were covered with CNTs. Secondly, patterning offers openings for vapor to exit the wick separately from the fluid-feeding capillary pores. Boiling performance is influenced by the resistance to the release of vapor generated at the base of the wick. This latter hypothesis of increased vapor permeability is assessed by testing a patterned sample without CNT coating.

Boiling curves comparing the patterned and homogeneous sintered samples are shown in Figure 10a. As expected, their performance is nearly identical in the evaporation regime since there is no vapor generation from the base of the wick. The patterned sample exhibits incipience superheat associated with a transition to boiling similar to that of the uncoated sample. An instantaneous temperature drop of 5.6 °C (versus 6.4 °C) is observed upon boiling incipience during this transition when the heat flux is changed from 45.3 to 59.9 W cm^{-2}. Following incipience, the enhancement provided by the patterning is apparent throughout the boiling regime once vapor generation from the base of the wick becomes the dominant mode of heat removal. The slope of the boiling curve is shifted toward lower substrate temperatures with a maximum superheat temperature decrease of 30 % observed at 514 W cm^{-2}. Based on *in situ* visualization of the sample surface, this significant reduction in substrate temperature is attributed to the hypothesized increase in vapor permeability due to patterning. Figure 10b shows a photograph of the central four open grid cells on the patterned sample during boiling. In this image two vapor bubbles are shown nucleating from the open grid areas. This is dissimilar from the homogeneous sample where vapor is forced to exit from the finer sintered powder capillary pores. Clearly, vapor preferentially agglomerates and exits the wick structure through these large open vents, increasing boiling efficacy. While CNT coating on the homogeneous sintered sample resulted in only low-end heat flux enhancement (as observed for Sample B in Figure 9a), micropatterning reduces the thermal resistance at the higher heat fluxes corresponding to vigorous boiling, and therefore displays the potential for extending the maximum supported input heat flux. An increase in boiling critical heat flux due to implementation of open vapor channels in a porous wick agrees with analytical models in the literature [43,44].

Sample D, which combines micropatterning and CNT coating of the sintered powder layer, is also compared against the baseline sample A in Figure 10a. Inspection of the boiling curves shows that the two separate enhancement mechanisms individually identified from testing samples B and C are preserved for sample D. The incipience overshoot is eliminated, resulting in a 58.4% reduction of the superheat temperature at 54.2 W cm^{-2} relative to sample A. In addition, the superheat is reduced by up to 29.4% at the higher heat fluxes as well. Encapsulating both of these significant performance augmentation strategies within a single evaporator structure is a noteworthy achievement made possible by engineering of CNT-integrated wick surfaces. Despite the elimination of incipience superheat by means of CNT coating, comparison between the CNT-coated patterned sample D and uncoated patterned sample C reveals slightly reduced thermal performance of the CNT-coated surface at intermediate heat fluxes from approximately 150 to 250 W cm^{-2}. Visualization of the sample surfaces during boiling does not reveal a significant difference in boiling behavior in this regime which could explain the slight performance reduction.

CONCLUSIONS

Combined micro- and nano-scale surface structuring for enhancement of both evaporation and boiling heat transfer from porous wick structures was proposed and verified in the current study. Controlled synthesis of a CNT array on a sintered copper powder microwick was shown to form a permeable nanoporous coating over the top layer of copper particles. Additionally, physical vapor deposition of copper over this CNT array yielded a uniform copper coating on each nanotube which resulted in a hydrophilic wicking surface viable for incorporation into vapor chambers utilizing water as the working fluid. The heat transfer enhancement provided by a CNT coating was confirmed using a test facility that replicates the internal conditions of a working vapor chamber. The CNT coating was shown to reduce the surface superheat temperature by as much as 72% by initiating boiling at low heat fluxes and avoid the boiling incipience temperature overshoot observed for uncoated samples. Finally, micropatterning of the sintered copper powder directly above the heat input area was shown to reduce the superheat temperature by up to 30% at high heat fluxes by creating high-permeability vents through which vapor generated during vigorous boiling could more readily leave the surface.

ACKNOWLEDGEMENTS

This material is based upon work supported by the Defense Advanced Research Projects Agency (DARPA) and Space and Naval Warfare Systems Center (SPAWAR/SYSCEN) San Diego, CA under Contract No. N66001-08-C-2011.

REFERENCES

1. S. Iijima, Helical Microtubules of Graphitic Carbon, *Nature*, vol. 354**,** pp. 56-58, 1991.
2. S. Berber, Y-K. Kwon, and D. Tomanek, Unusually High Thermal Conductivity of Carbon Nanotubes, *Physical Review Letters*, vol. 84, pp. 4613-4616, 2000.
3. J. Che, T. Cagin, and W.A. Goddard, Thermal Conductivity of Carbon Nanotubes, *Nanotechnology*, vol. 11**,** pp. 65-69, 2000.
4. P. Kim, L. Shi, A. Majumdar, and P.L. McEuen, Thermal Transport Measurements of Individual Multiwalled Nanotubes, *Physical Review Letters*, vol. 87, pp. 215502/1-4, 2001.
5. M. Fujii, X. Zhang, and K. Takahashi, Measurements of Thermal Conductivity of Individual Carbon Nanotubes, *Physica Status Solidi B*, vol. 243, pp. 3385-3389, 2006.
6. A.E. Aliev, M.H. Lima, E.M. Silverman, and R.H. Baughman, Thermal Conductivity of Multi-walled Carbon Nanotube Sheets: Radiation Losses and Quenching of Phonon Modes, *Nanotechnology*, vol. 21, pp. 035709/1-11, 2010.
7. E. Pop, D. Mann, Q. Wang, K. Goodson, and H. Dai, Thermal Conductance of an Individual Single-wall Carbon Nanotube above Room Temperature, *Nano Letters*, vol. 6, pp. 96-100, 2006.
8. M.S. Dresselhaus and P.C. Eklund, Phonons in Carbon Nanotubes, *Advances in Physics*, vol. 49, pp. 705-814, 2000.
9. P.B. Amama, B.A. Cola, T.D. Sands, X. Xu, and T.S. Fisher, Dendrimer-assisted Controlled Growth of Carbon Nanotubes for Enhanced Thermal Interface Conductance, *Nanotechnology*, vol. 18, pp. 385303/1-4, 2007.
10. B.A. Cola, J. Xu, C. Cheng, X. Xu, T.S. Fisher, and H. Hu, Photoacoustic Characterization of Carbon Nanotube Array Thermal Interfaces, *Journal of Applied Physics*, vol. 101, pp. 054313/1-9, 2007.

11. P.B. Amama, C. Lan, B.A. Cola, X. Xu, R.G. Reifenberger, and T.S. Fisher, Electrical and Thermal Interface Conductance of Carbon Nanotubes Grown Under Direct Current Bias Voltage, *The Journal of Physical Chemistry C*, vol. 112, pp. 19727-19733, 2008.

12. B.A. Cola, X. Xu, T.S. Fisher, and M.A. Capano, Carbon Nanotube Array Thermal Interfaces for High-Temperature Silicon Carbide Devices, *Nanoscale and Microscale Thermophysical Engineering*, vol. 12, pp. 228-237, 2008.

13. H. Wang, J. Feng, X. Hu, and K.M. Ng, Synthesis of Aligned Carbon Nanotubes on Double-sided Metallic Substrate by Chemical Vapor Deposition, *The Journal of Physical Chemistry C*, vol. 111, pp. 12617-12624, 2007.

14. M.J. Biercuk, M.C. Llaguno, M. Radosavljevic, J.K. Hyun, A.T. Johnson, and J.E. Fischer, Carbon Nanotube Composites for Thermal Management, *Applied Physics Letters*, vol. 80, pp. 2767-2769, 2002.

15. C.H. Liu, H. Huang, Y. Wu, and S.S. Fan, Thermal Conductivity Improvement of Silicone Elastomer with Carbon Nanotube Loading, *Applied Physics Letters*, vol. 84, pp. 4248-4250, 2004.

16. Q. Ngo, B.A. Cruden, A.M. Cassell, G. Sims, M. Meyyappan, J. Li, and C.Y. Yang, Thermal Interface Properties of Cu-filled Vertically Aligned Carbon Nanofiber Arrays, *Nano Letters*, vol. 4, pp. 2403-2407, 2004.

17. H. Li, C. Liu, and S. Fan, Catalyzed Filling of Carbon Nanotube Array with Graphite and the Thermal Properties of the Composites, *The Journal of Physical Chemistry C*, vol. 112, pp. 5840-5842, 2008.

18. H.S. Ahn, N. Sinha, M. Zhang, D. Banerjee, S. Fang, and R.H. Baughman, Pool Boiling Experiments on Multiwalled Carbon Nanotube (MWCNT) Forests, *Journal of Heat Transfer*, vol. 128, pp. 1335-1342, 2006.

19. V. Sathyamurthi, H.S. Ahn, D. Banerjee, and S.C. Lau, Subcooled Pool Boiling Experiments on Horizontal Heaters Coated with Carbon Nanotubes, *Journal of Heat Transfer*, vol. 131, pp. 71501/1-10, 2009.

20. S. Ujereh, T. Fisher, and I. Mudawar, Effects of Carbon Nanotube Arrays on Nucleate Pool Boiling, *International Journal of Heat and Mass Transfer*, vol. 50, pp. 4023-4038, 2007.

21. S. Launay, A.G. Fedorov, Y. Joshi, A. Cao, and P.M. Ajayan, Hybrid Micro-nano Structured Thermal Interfaces for Pool Boiling Heat Transfer Enhancement, *Microelectronics Journal*, vol. 37, pp. 1158-1164, 2006.

22. C. Li, Z. Wang, P. Wang, Y. Peles, N. Koratkar, and G. P. Peterson,. Nanostructured Copper Interfaces for Enhanced Boiling, *Small*, vol. 4, pp. 1084-1088, 2008.

23. J.A. Weibel, S.V. Garimella, and M.T. North, Characterization of Evaporation and Boiling from Sintered Powder Wicks fed by Capillary Action, *International Journal of Heat and Mass Transfer*, vol. 53, pp. 4204-4215, 2010.

24. C. Li, G.P. Peterson, and Y. Wang, Evaporation/Boiling in Thin Capillary Wicks (l)-Wick Thickness Effects, *Journal of Heat Transfer*, vol. 128, pp. 1312-1319, 2006.

25. C. Li and G.P. Peterson, Evaporation/Boiling in Thin Capillary Wicks (II)-Effects of Volumetric Porosity and Mesh Size, *Journal of Heat Transfer*, vol. 128, pp. 1320-1328, 2006.

26. T. Semenic and I. Catton, Experimental Study of Biporous Wicks for High Heat Flux Applications, *International Journal of Heat and Mass Transfer*, vol. 52, pp. 5113-5121, 2009.

27. T. Werder, J.H. Walther, R.L. Jaffe, T. Halicioglu, F. Noca, and P. Koumoutsakos, Molecular Dynamics Simulation of Contact Angles of Water Droplets in Carbon Nanotubes, *Nano Letters*, vol. 1, pp. 697-702, 2001.

28. A.H. Barber, S.R. Cohen, and H.D. Wagner, Static and Dynamic Wetting Measurements of Single Carbon Nanotubes, *Physical Review Letters*, vol. 92, pp. 186103/1-4, 2004.

29. L. Feng, S. Li, Y. Li, H. Li, L. Zhang, J. Zhai, Y. Song, B. Liu, L. Jiang, and D. Zhu, Super-hydrophobic Surfaces: From Natural to Artificial, *Advanced Materials*, vol. 14, pp. 1857-1860, 2002.

30. W.C. Poh, K.P. Loh, W.D. Zhang, S. Triparthy, J-S. Ye, and F-S. Sheu, Biosensing Properties of Diamond and Carbon Nanotubes, *Langmuir*, vol. 20, pp. 5484-5492, 2004.

31. J.J. Zhou, F. Noca, and M. Gharib, Flow Conveying and Diagnosis with Carbon Nanotube Arrays, *Nanotechnology*, vol. 17, pp. 4845-4853, 2006.

32. F. Wang, S. Arai, and M. Endo, Ni-fluorinated Vapor Growth Carbon Fiber (VGCF) Composite Films Prepared by an Electrochemical Deposition Process, *Electrochemistry Communications*, vol. 6, pp. 1042-1044, 2004.

33. Y. Peng and Q. Chen, The Synthesis of a Copper/Multi-walled Carbon Nanotube Hybrid Nanowire in a Microfluidic Reactor, *Nanotechnology*, vol. 20, pp. 235606/1-7, 2009.

34. S.S. Kim, J.A. Weibel, T.S. Fisher, and S.V. Garimella, Thermal Performance of Carbon Nanotube Enhanced Vapor Chamber Wicks, *Proceedings of the 14th International Heat Transfer Conference*, IHTC14-22929, 2010.

35. J.A. Weibel, S.V. Garimella, J.Y. Murthy, and D.H. Altman, Design of Integrated Nanostructured Wicks for High-Performance Vapor Chambers, *IEEE Transactions on Components and Packaging Technologies*, Preprint Accepted Paper. (NEED TO UPDATE REFERENCE)

36. R.K. Garg, S.S. Kim, D.B. Hash, J.P. Gore, and T.S. Fisher, Effects of Feed Gas Composition and Catalyst Thickness on Carbon Nanotube and Nanofiber Synthesis by Plasma Enhanced Chemical Vapor Deposition, *Journal of Nanoscience and Nanotechnology*, vol. 8, pp. 3068-3076, 2008.

37. S.S. Kim, P.B. Amama, and T.S. Fisher, Preferential Biofunctionalization of Carbon Nanotubes Grown by Microwave Plasma-Enhanced CVD, *The Journal of Physical Chemistry C*, vol. 114, pp. 9596-9602, 2010.

38. T. Yamada, T. Namai, K. Hata, D.N. Futaba, K. Mizuno, J. Fan, M. Yudasaka, M. Yumura, and S. Iijima, Size-Selective Growth of Double-Walled Carbon Nanotube Forests from Engineered Iron Catalysts, *Nature Nanotechnology*, vol. 1, pp. 131-136, 2006.

39. N.R. Wilson, and J.V. Macpherson, Carbon Nanotube Tips for Atomic Force Microscopy, *Nature Nanotechnology*, vol. 4, pp. 483-491, 2009.

40. L. Zheng, G. Sun, and Z. Zhan, Tuning Array Morphology for High-Strength Carbon-Nanotube Fibers, *Small*, vol. 6, pp. 132-137, 2010.

41. A. Faghri, Heat Pipe Science and Technology, Taylor & Francis, Washington, D.C., 1995.

42. K.K. Bodla, J.Y. Murthy, and S.V. Garimella, Direct Simulation of Thermal Transport through Sintered Wick Microstructures, *Journal of Heat Transfer*, Paper in production, No. HT-11-1042.

43. A.K. Stubos and J-M. Buchlin, Enhanced Cooling via Boiling in Porous Layers: The Effect of Vapor Channels, *Journal of Heat Transfer*, vol. 121, pp. 205-210, 1999.

44. W. Wei, D. Jian-Hua, and W. Bu-Xuan, Boiling Heat Transfer on Surfaces Coated by Porous Wick with Vapor Channels, *Nanoscale and Microscale Thermophysical Engineering*, vol. 5, pp. 277-284, 2001.

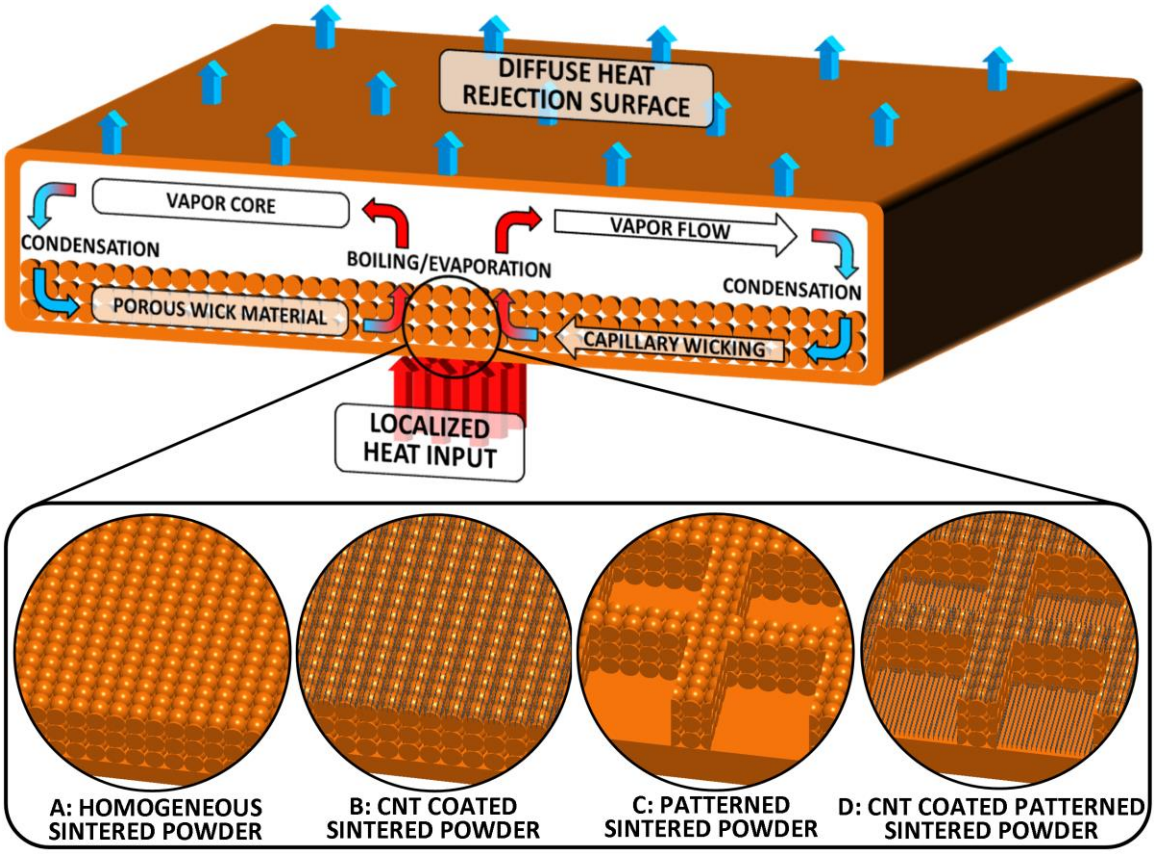

Figure 1 Schematic operation of a vapor chamber heat spreading device showing the internal transport processes. An inset view of the evaporator microgeometry depicts the four fabricated test surfaces investigated in the current study.

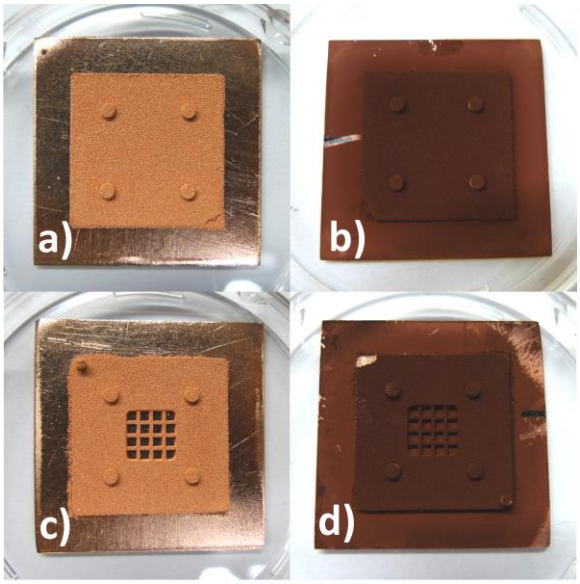

Figure 2 a) Uncoated homogeneous sample, b) CNT-coated homogeneous sample, c) uncoated patterned sample, and d) CNT-coated patterned sample.

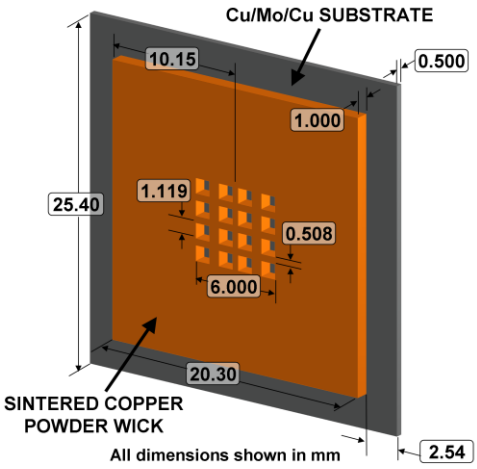

Figure 3 Illustration of the grid-patterned evaporator sample (sample C), including the substrate and sintered copper powder dimensions. Dimensions of the uniform homogeneous evaporator sample (sample A) are identical but lack the central grid features. The porous wick is bonded to the substrate during the sintering process.

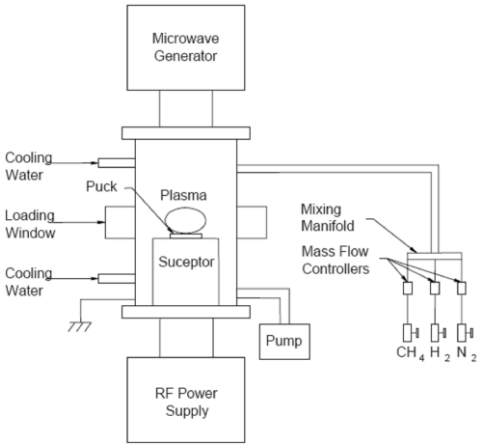

Figure 4 Schematic diagram of microwave plasma chemical vapor deposition (MPCVD) system.

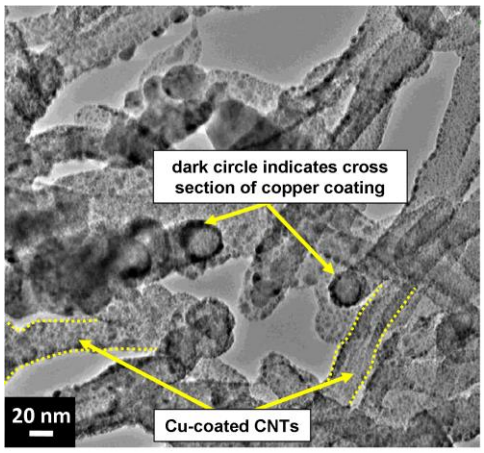

Figure 5 TEM image of CNTs coated with Cu.

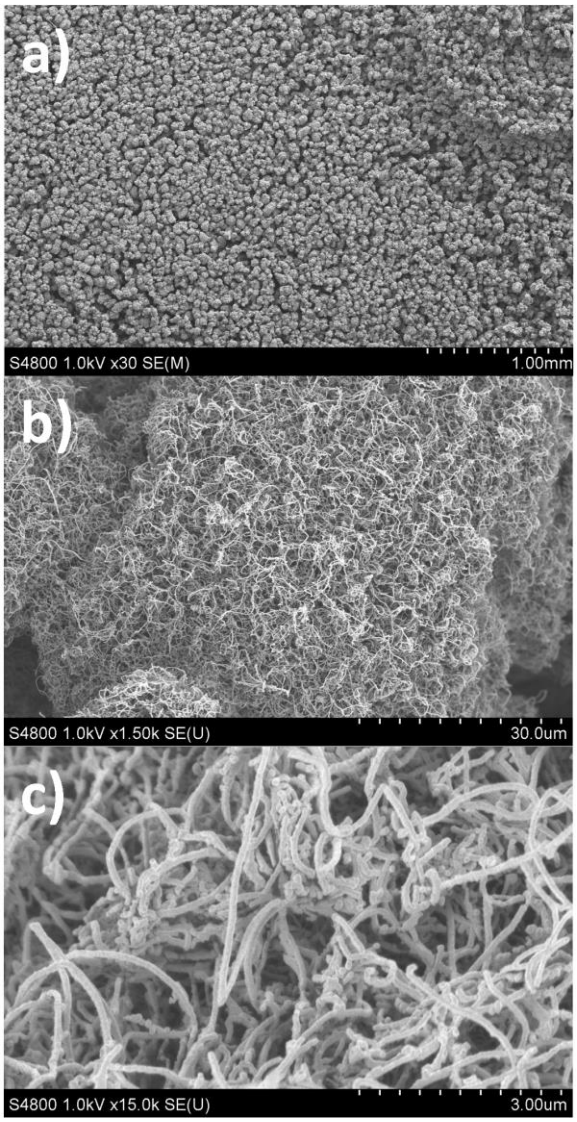

Figure 6 a) Low, b) medium, and c) high magnification SEM images of the CNT-coated homogeneous sample with evaporated Cu coating.

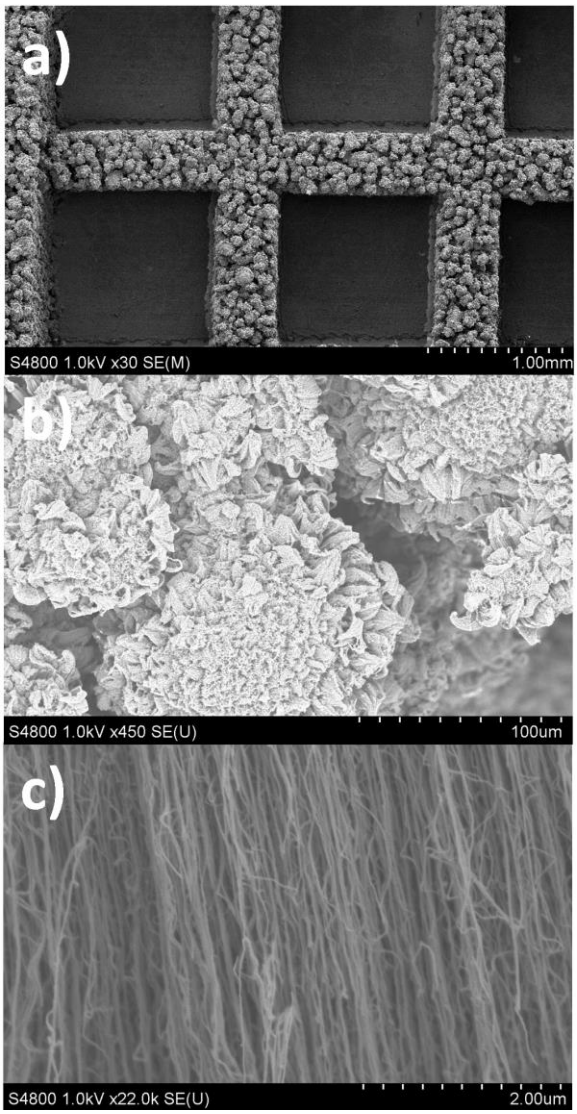

Figure 7 a) Low, b) medium, and c) high magnification SEM images of CNT-coated patterned sample prior to deposition of Cu.

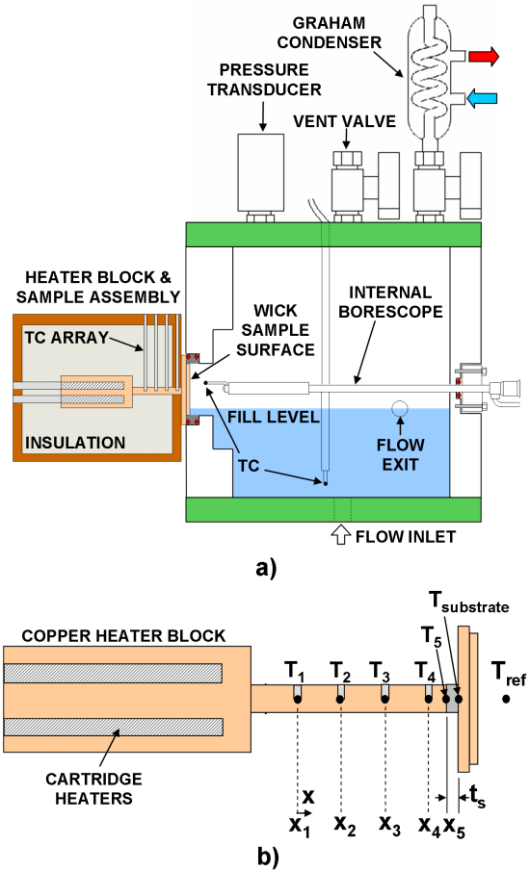

Figure 8 a) Schematic diagram of the capillary-fed boiling experimental facility showing the saturated test chamber, and b) detailed illustration of the copper heater block temperature measurements used to determine the input heat flux and substrate temperature.

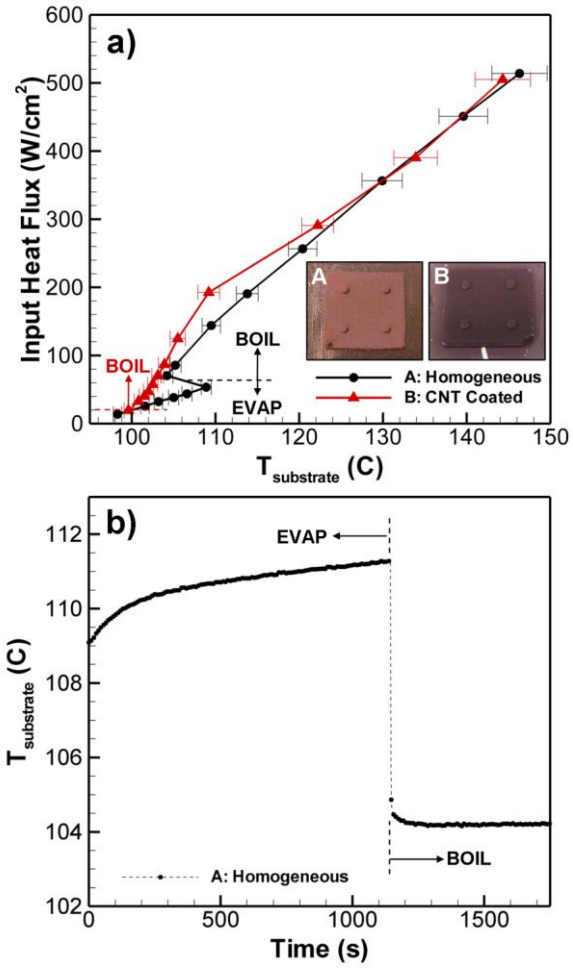

Figure 9 a) Boiling curves comparing the CNT-coated uniform homogeneous sintered powder sample B against the baseline uncoated sample A. Boiling (BOIL) and evaporation (EVAP) regimes are identified. Uncertainty in input heat flux is less than ± 5 W cm^{-2}. b) Transient substrate temperature response of sample A for the transition from 53.4 to 70.4 W cm^{-2}, which depicts a near instantaneous boiling incipience temperature drop.

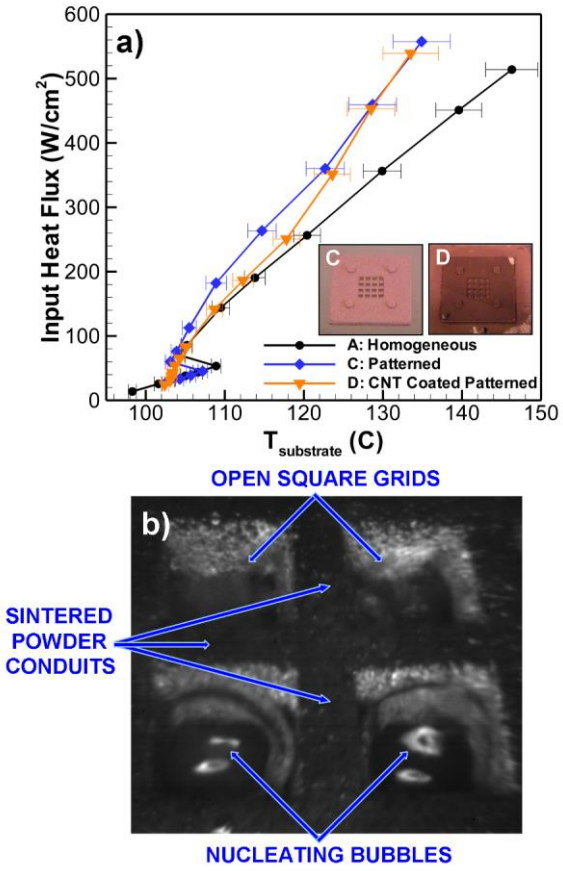

Figure 10 a) Boiling curves comparing the uncoated patterned sample C and the CNT-coated patterned sample D against the baseline uncoated homogeneous sample A. Uncertainty in input heat flux is less than ± 5 W cm^{-2}. b) *In situ* image of boiling from the patterned sintered copper powder evaporator structure.